

# Ferroelectric control of magnetization in $\text{La}_{1-x}\text{Sr}_x\text{MnO}_3$ manganites: A first-principles study

Hanghui Chen<sup>1,3</sup> and Sohrab Ismail-Beigi<sup>1,2,3</sup>

<sup>1</sup>*Department of Physics, Yale University,  
New Haven, Connecticut, 06511, USA*

<sup>2</sup>*Department of Applied Physics, Yale University,  
New Haven, Connecticut, 06511, USA*

<sup>3</sup>*Center for Research on Interface Structures and Phenomena (CRISP),  
Yale University, New Haven, CT 06511, USA*

(Dated: November 2, 2018)

## Abstract

We present a first-principles study on the interface between perovskite ferroelectrics ( $\text{PbTiO}_3$ ) and conducting magnetic manganites ( $\text{La}_{1-x}\text{Sr}_x\text{MnO}_3$ ). We show that by switching the ferroelectric polarization, additional carriers are accumulated or depleted at the interfacial region of the manganite and that this change in carrier density can modify the magnetic spin configuration of the interfacial Mn, which is consistent with the experimentally observed anomalously large change in the magnetization. We also describe an unexpected purely interfacial phenomenon whereby the ferroelectric polarization of the interfacial region changes the magnetic energetics — a degree of freedom not present in bulk manganites. Theoretically, we show the the ground-state magnetic structure depends sensitively on the precise choice of Hubbard  $U$  parameter within the widely-used DFT+ $U$  class of exchange correlation functionals. We provide a simple Ising-like model that explains the evolution of the magnetic structure with  $U$  in tandem with a discussion of various different ways in which one might try to choose an appropriate  $U$  parameter.

## I. INTRODUCTION

Multiferroics have been one of the most intensively studied materials during the past decade [1, 2]. The coexistence of more than one order parameter in a single phase and their coupling may open new routes to the next generation of electronic devices. For instance, the possibility of controlling magnetization via external electric fields may find promising applications in spintronics. The origin of magnetoelectric multiferroicity lies in a nonzero magnetoelectric coupling which may occur due to many different mechanisms (for recent reviews, see [3, 4]). The magnetic properties of an intrinsic bulk magnetoelectric, of which  $\text{Cr}_2\text{O}_3$  is a prototype, can be modulated by an external field through the change of the magnetic cations' displacement relative to anions [5]. Extrinsic magnetoelectric couplings are typically mediated by strain: in composites of piezomagnetic materials combined with electrostrictive materials, external fields modulate the electric polarization, as well as the shape of the piezoelectric. This change in turn induces strain of the magnetic components and modifies the magnetization in the magnetostrictive material [6].

However, although these bulk mechanisms are well understood, the magnitude of magnetoelectric couplings in bulk materials is generally small [7], impeding their applications in electronic devices. Moving away from bulk materials, artificial heterostructures such as interfaces are promising candidates for realizing or even engineering magnetoelectric couplings. Recently, a variety of mechanisms were proposed to induce magnetoelectric coupling at interfaces. At ferromagnet/ferroelectric interfaces, the interfacial bond length can be altered by the presence of ferroelectric polarization, for example in  $\text{Fe}/\text{BaTiO}_3$  [8],  $\text{Co}_2\text{MnSi}/\text{BaTiO}_3$  [9] and  $\text{Fe}_3\text{O}_4/\text{BaTiO}_3$  [10]. Another mechanism is to apply an external field and induce magnetization mediated by free screening carriers accumulated at ferromagnetic/dielectric interfaces, for example  $\text{SrRuO}_3/\text{SrTiO}_3$  [11]. A more complex but intriguing mechanism was recently described theoretically and experimentally [12, 13] at ferroelectric/conducting magnetic manganite interfaces. Our work focuses on this last class of systems, because the coupling between ferroelectric polarization and magnetization not only is of great importance in fundamental sciences, but also finds very promising applications in memory devices [14, 15].

At a ferroelectric/manganite interface, the presence of the ferroelectric polarization causes screening charges to appear at the interface due to accumulation or depletion of carriers in the

interfacial region. Much like SrRuO<sub>3</sub>/SrTiO<sub>3</sub> interfaces, the magnetization of the interfacial atoms can be enhanced due to the modification of carrier density around the interface because the magnetic moment of the atoms depends on the doping level (provided that the manganite is in the ferromagnetic phase). What is different in the ferroelectric/manganite system is that the accumulation of carriers not only changes the magnetic moment but can lead to an interfacial ferromagnetic-to-antiferromagnetic transition which reverses the directions of the moments and thus to a much larger magnetoelectric coupling. The work of Ref. [12] studied a representative heterostructure: BaTiO<sub>3</sub>/La<sub>1-x</sub>Ba<sub>x</sub>MnO<sub>3</sub> with  $x = 0.5$ . For bulk La<sub>1-x</sub>Sr<sub>x</sub>MnO<sub>3</sub>,  $x = 0.5$  is at the critical doping level separating ferromagnetic and antiferromagnetic phases, so the system is highly susceptible to magnetic changes with small changes of doping. What was found is that when the ferroelectric polarization is flipped, the magnetic moment of the Mn atoms in the second unit cell away from the interface is reversed. We note that the result is somewhat unintuitive as the carrier doping density is highest in the first layer at the interface which is most susceptible to change of magnetic phase. Experiments on the Pb(Ti<sub>0.8</sub>Zr<sub>0.2</sub>)O<sub>3</sub>/La<sub>1-x</sub>Sr<sub>x</sub>MnO<sub>3</sub> are performed for  $x = 0.2$  [13] which is quite far from the boundary: *a priori* it is not clear whether enough screening charges can accumulate to drive the system over the magnetic phase transition. The experiments find a large magneto-electric coupling which is interpreted to originate from a spin-flip in the first unit cell of the manganite closest to the interface [13].

In this work, we comprehensively study this proposed magnetoelectric phenomenon at the ferroelectric/manganite interface using first-principles calculations. We choose PbTiO<sub>3</sub>/La<sub>1-x</sub>Sr<sub>x</sub>MnO<sub>3</sub> as our prototype for computational convenience. Although the experiments use Pb(Ti<sub>0.8</sub>Zr<sub>0.2</sub>)O<sub>3</sub> as the ferroelectric [13] in order to reduce leakage currents, the key role of the ferroelectric is to induce screening charges due to its surface polarization, and we believe the compositional details are secondary. For the La<sub>1-x</sub>Sr<sub>x</sub>MnO<sub>3</sub> thin film, we choose the nominal hole doping to be  $x = 0.2$  (unless otherwise specified) in order to directly compare to experiment [13].

The original contributions of this paper are the following. (i) We are able to show that even though the manganite film has a low nominal doping of  $x = 0.2$ , the ferroelectric field effects can sufficiently change the carrier density to induce a magnetic transition at the interface. However, the precise ground-state magnetic structure of the interface (e.g., no spin-flip, spin-flip in first Mn layer, spin-flip in second Mn layer) depends sensitively on the choice

of exchange correlation functionals and specifically the value of the Hubbard  $U$  parameter in the DFT+ $U$  approach. (ii) We clarify the physical reasons of the sensitivity based on a simple Ising-like nearest-neighbor model using bulk-derived parameters that well describes the computed dependences. (iii) We describe an unexpected purely interfacial effect that significantly modifies the energies of magnetic states at the interface: the ferroelectric polarization propagates into the first few manganite layers and the resulting rumplings of atomic layers are responsible for the modifications. This degree of freedom is not present in the bulk and potentially represents a further degree of freedom that can be exploited to modify and engineer material properties at oxide interfaces. (iv) We show that various approaches to find an appropriate  $U$  produce significantly different  $U$  values, some of which do poorly when used to compute results that compare to bulk properties of manganites; empiricism in the choice of  $U$  is an unfortunate necessity for manganites using state-of-the-art *ab initio* methods. (v) In the process of this work, we develop an alternative method for counting electrons on the Mn atoms in  $\text{La}_{1-x}\text{Sr}_x\text{MnO}_3$  thin films that is directly based on the electron density instead of the standard and widely used method based on projecting onto Löwdin or atomic-like orbitals [16]. With this method, we can quantify the carrier distribution as a function of ferroelectric polarization and calculate the layer-resolved effective hole doping. The method is generally applicable to half-metallic oxide films.

The remainder of the paper is organized as follows. We discuss computational details in Section II. We first study the magnetic phase transition of bulk  $\text{La}_{1-x}\text{Sr}_x\text{MnO}_3$  in Section III A. A discussion of Hubbard  $U$  for bulk  $\text{La}_{1-x}\text{Sr}_x\text{MnO}_3$  is presented in Section III B. The charge modulation at the interface is studied in Section IV B and Section IV C is devoted to the discussion of spin modulation at the interface. We conclude in Section V. A number of appendices contain further technical details.

## II. COMPUTATIONAL DETAILS

Our calculations are performed using density functional theory within the *ab initio* supercell plane-wave approach [17], with the code PWscf in the Quantum-ESPRESSO package [38]. We employ ultrasoft pseudopotentials [18]. The semicore states and reference configuration of each element are shown in Table I. We use the local spin density approximation (LSDA) [19] for the exchange correlation functional as well as the Hubbard  $U$  correction

TABLE I: The semicore states and reference configurations of our pseudopotentials. The cut-off radii are in units of Bohr.

Atom	Reference valence states	$r_c^s$	$r_c^p$	$r_c^d$
Pb	$5d^{10}6s^26p^2$	2.5	2.5	2.3
Ti	$3s^23p^63d^14s^2$	1.8	1.8	1.8
Sr	$4s^24p^65s^2$	2.0	1.8	2.0
La	$5s^25p^65d^16s^{1.5}6p^{0.5}$	2.2	2.0	2.2
Mn	$3s^23p^63d^54s^2$	2.0	2.0	2.0
Pt	$5d^96s^16p^0$	1.0	1.0	1.2
O	$2s^22p^4$	1.3	1.3	–

method (LSDA+ $U$ ) [20] to account for some of the strong electronic correlations on the localized  $d$  orbitals of Mn atoms. The plane wave basis energy cutoff and charge cutoff are 35 Ry and 280 Ry, respectively. We use a Gaussian smearing width of 5 mRy when sampling the Brillouin zone. For bulk  $\text{La}_{1-x}\text{Sr}_x\text{MnO}_3$ , the  $k$ -grid sampling of the Brillouin zone is  $20 \times 20 \times 20$  per formula unit. For interface calculations, the  $k$ -grid sampling is  $20 \times 20 \times 2$  where the  $z$ -axis is orthogonal to the interface. For variable cell relaxations, the convergence threshold for pressure is 0.5 Kbar. For atom relaxations, the convergence threshold for every force component is 26 meV/Å. We have checked the convergence in total energies and structural parameters by further increasing the  $k$ -point sampling and reducing the stress and force threshold, and observe no significant differences in key physical observables.

The  $A$ -site  $\text{La}_{1-x}\text{Sr}_x$  alloying is treated by the virtual crystal approximation [21, 22]. Appendix A describes tests on the accuracy of the virtual crystal approximation for our system: the results are highly satisfactory and consistent with earlier observations [23]

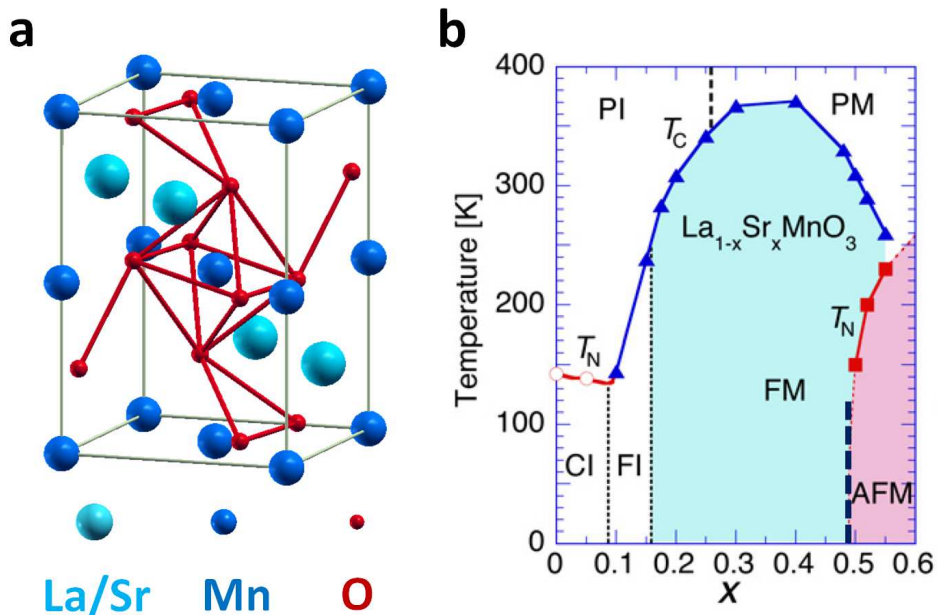


FIG. 1: (Color online) **a**) 20-atom unit cell of  $Pnma$   $\text{La}_{1-x}\text{Sr}_x\text{MnO}_3$ . **b**) Experimental phase diagram of  $\text{La}_{1-x}\text{Sr}_x\text{MnO}_3$ . ‘CI’ means canted insulating. ‘FI’ means ferromagnetic insulating. ‘FM’ means ferromagnetic metallic. ‘AFM’ means antiferromagnetic metallic. ‘PI’ means paramagnetic insulating. ‘PM’ means paramagnetic metallic. The phase boundary of the ferromagnetic to  $A$ -type antiferromagnetic phase transition at low temperatures is highlighted by the bold dashed line. The panel **b**) is reproduced with permission from Ref. [27]. Copyright 2006 Institute of Physics Publishing.

### III. BULK MANGANITES

#### A. Phase transition of magnetic ordering

Since, as we will show, the magnetic properties of  $\text{PbTiO}_3/\text{La}_{1-x}\text{Sr}_x\text{MnO}_3$  interface can be understood qualitatively in terms of bulk  $\text{La}_{1-x}\text{Sr}_x\text{MnO}_3$ , we start the discussion with the phase diagram of bulk  $\text{La}_{1-x}\text{Sr}_x\text{MnO}_3$  under different conditions. The parent compound of  $\text{La}_{1-x}\text{Sr}_x\text{MnO}_3$  is  $\text{LaMnO}_3$  which is an  $A$ -type antiferromagnetic Mott insulator [24]. Bulk  $\text{LaMnO}_3$  has strong Jahn-Teller and  $\text{GdFeO}_3$  distortions with  $Pnma$  symmetry [25] and its primitive cell is of size  $c(2 \times 2) \times 2$  in units of the cubic perovskite. The smallest unit cell of  $\text{LaMnO}_3$  has four formula units (20 atoms), as is illustrated in Fig. 1a. Chemically doping  $\text{LaMnO}_3$  with Sr induces holes on the Mn  $d$ -orbitals, leading to conduction and various

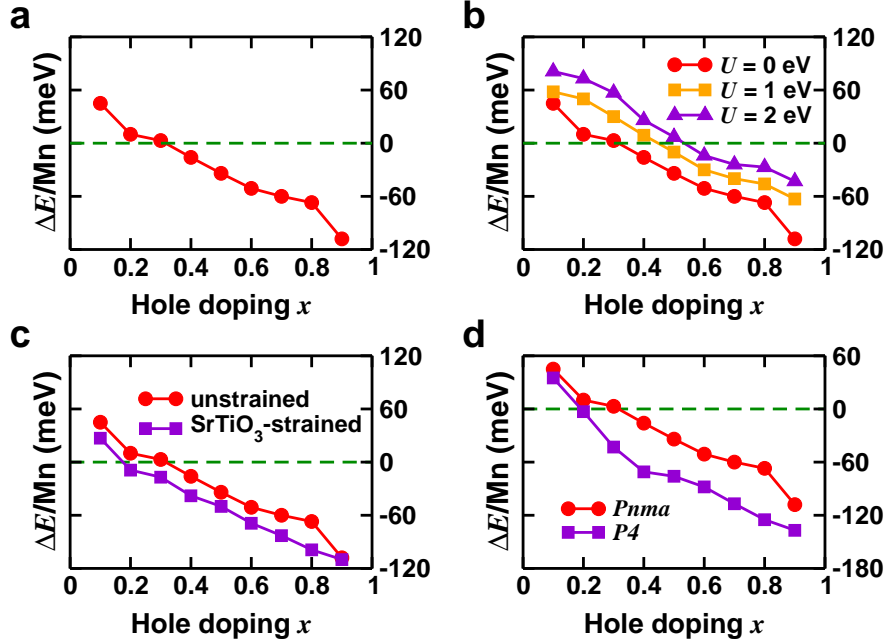


FIG. 2: (Color online) Phase diagram of bulk  $Pnma$   $\text{La}_{1-x}\text{Sr}_x\text{MnO}_3$ .  $\Delta E$  is defined in Eq. (1). Above zero, the ground state is ferromagnetic and below zero it is  $A$ -type antiferromagnetic. **a)** Hole doping dependence within LSDA. **b)** Hubbard  $U$  dependence. **c)** Strain dependence. **d)** Structural distortion dependence.

magnetic orderings. Fig. 1b shows the experimental phase diagram of bulk  $\text{La}_{1-x}\text{Sr}_x\text{MnO}_3$ . A ferromagnetic to  $A$ -type antiferromagnetic phase transition occurs around  $x = 0.5$  doping, which is highlighted by the bold dashed line in Fig. 1b. For a random alloy distribution, we assume that bulk  $\text{La}_{1-x}\text{Sr}_x\text{MnO}_3$  has the same symmetry as  $\text{LaMnO}_3$  ( $Pnma$ ). In DFT simulations, we replace La with the fictitious atom  $\text{La}_{1-x}\text{Sr}_x$  in the virtual crystal approximation and calculate the energy difference between ferromagnetic ordering ( $F$ ) and  $A$ -type antiferromagnetic ordering ( $A$ ) as a function of doping  $x$ .

$$\Delta E = E(A) - E(F) \quad (1)$$

In addition to the doping dependence  $x$ , we also study the effect of strain, structural distortions and Hubbard  $U$  on the magnetic transition of bulk  $\text{La}_{1-x}\text{Sr}_x\text{MnO}_3$ .

### 1. Doping dependence

Fig. 2a shows a representative bulk phase diagram of  $\text{La}_{1-x}\text{Sr}_x\text{MnO}_3$  as a function of doping  $x$ . The calculation is performed in the LSDA (i.e. Hubbard  $U=0$ ). DFT-LSDA reproduces the ferromagnetic-to-antiferromagnetic phase transition that is observed in experiment. The doping dependence can be understood as follows: the ferromagnetic ordering is stabilized by the double exchange mechanism which relies on the hopping of the lone  $e_g$  electrons among the  $\text{Mn}^{3+}$  ions [26]. With the increasing hole doping  $x$ , the itinerant electrons (i.e.  $\text{Mn}^{3+}$  ions) are drained and the hopping processes are suppressed. Therefore the double exchange mechanism becomes less operative and the ferromagnetic ordering gets more unstable as  $x$  is increased. We need to point out that in the experimental phase diagram for  $x < 0.1$ ,  $\text{La}_{1-x}\text{Sr}_x\text{MnO}_3$  is a spin-canted insulator (a magnetic structure close to  $A$ -type antiferromagnetic ordering but the magnetic moment is not exactly cancelled due to weak spin-canting) [27]. As  $x$  increases to 0.2, there is an insulating-to-metallic transition and the appearance of the ferromagnetic ordering which is not reproduced in the DFT-LSDA calculation, since the LSDA ground state is metallic in the whole doping range. Turning on the Hubbard  $U$  does not change the metallicity of ferromagnetic  $\text{La}_{1-x}\text{Sr}_x\text{MnO}_3$ . We argue that even though LSDA or LSDA+ $U$  is not accurate enough to reproduce the spin-canted ground state at very low doping nor the insulating-to-metallic transition around  $x \simeq 0.2$ , it correctly produces the metallic ferromagnetic to metallic antiferromagnetic phase transition at larger  $x$ , which is the key to understanding the spin-modified magnetic structure of manganites in the presence of ferroelectrics.

### 2. Hubbard $U$ dependence

Fig. 2b shows a comparison of LSDA and LSDA+ $U$  calculations for bulk  $\text{La}_{1-x}\text{Sr}_x\text{MnO}_3$ . The ferromagnetic-to-antiferromagnetic phase transition is well reproduced in both LSDA and LSDA+ $U$  calculations, but the transition point, i.e. the critical hole density where the ground state changes magnetic ordering, depends on the value of the Hubbard  $U$ . With an increasing  $U$ , the transition point moves to larger doping values while the overall features of the transition remain unchanged. The Hubbard  $U$  dependence originates as follows: antiferromagnetism is favored by the superexchange mechanism which involves the virtual



hopping of electrons between low and high energy sites with the same spin [28]. A larger  $U$  increases the energy splitting and thus the virtual hopping is suppressed. Therefore the superexchange mechanism is suppressed as  $U$  increases, and the antiferromagnetic ordering accordingly becomes less stable, resulting in the upward shift of phase transition curve (favoring ferromagnetism). Empirically in order to correctly locate the transition point at the experimental value of  $x \simeq 0.5$ , we need a Hubbard  $U$  in the range of  $1 \text{ eV} < U < 2 \text{ eV}$  in the LSDA+ $U$  approximation (as illustrated in Fig. 2b).

### 3. Strain dependence

Since the  $\text{La}_{1-x}\text{Sr}_x\text{MnO}_3$  thin film is grown coherently on an  $\text{SrTiO}_3$  substrate, we also study the phase diagram of  $\text{SrTiO}_3$ -strained  $\text{La}_{1-x}\text{Sr}_x\text{MnO}_3$  and compare it with unstrained bulk  $\text{La}_{1-x}\text{Sr}_x\text{MnO}_3$  in Fig. 2c.  $\text{La}_{1-x}\text{Sr}_x\text{MnO}_3$  in the whole doping range is under weak tensile strain (within 1%) when on an  $\text{SrTiO}_3$  substrate. Tensile (compressive) strain removes the degeneracy of Mn  $e_g$  orbitals and favors  $d_{x^2-y^2}$  ( $d_{3z^2-r^2}$ ) orbitals due to the change of crystal field [29]. Based on the double exchange mechanism, ferromagnetism is isotropic with equal hoppings between Mn atoms along  $x$ ,  $y$  and  $z$  directions.  $A$ -type antiferromagnetism is ferromagnetic in-plane and alternates its spin orientation layer by layer along the out-of-plane axis [30]. Due to the tensile strain, the occupancy of  $d_{3z^2-r^2}$  is lowered and the hopping between Mn atoms becomes essentially two-dimensional, suppressing ferromagnetism. Therefore with tensile strain, ferromagnetism is destabilized and the whole transition curve is shifted downwards (favoring  $A$ -type antiferromagnetic ordering) as seen in Fig. 2c.

### 4. Structural distortions

Distortions away from cubic symmetry play a crucial role in the magnetism of manganites [31]. Bulk  $\text{La}_{1-x}\text{Sr}_x\text{MnO}_3$  has complicated structural distortions with  $Pnma$  symmetry (the unit cell is  $c(2 \times 2) \times 2$  with 20 atoms). However, we also theoretically study ‘artificial’  $\text{La}_{1-x}\text{Sr}_x\text{MnO}_3$  with only tetragonal distortions (the symmetry is  $P4$  and the unit cell is  $1 \times 1 \times 2$ ). The main reason we consider the high symmetry phase ( $P4$ ) and compare it to the low symmetry structure ( $Pnma$ ) is computational: the  $P4$  symmetry allows for the use of a smaller  $1 \times 1$  interface unit cell which allows for simulation of much thicker films and

substrates. Therefore we need to understand the main differences, if any, between the two phases for what follows below. In addition, a comparison allows us to elucidate the role of structural distortions.

Fig. 2d shows a representative phase diagram versus doping for both  $Pnma$   $\text{La}_{1-x}\text{Sr}_x\text{MnO}_3$  and  $P4$   $\text{La}_{1-x}\text{Sr}_x\text{MnO}_3$  in the LSDA approximation. To understand these results, we begin with the fact that the effective hopping matrix element  $t$  between neighbouring Mn atoms depends on the Mn-O-Mn bond angle [32]. In the  $P4$  case, the bond angle is  $180^\circ$  and the hopping is maximized, while in the  $Pnma$  case, the bond angle is smaller than  $180^\circ$  and the hopping is reduced. The double exchange mechanism depends linearly on this effective hopping matrix element  $t$ , while the superexchange mechanism lowers the energy of antiferromagnetism by  $\propto t^2$  from second-order perturbation theory [32]. Therefore as we increase the hopping matrix element  $t$ , superexchange is more significantly enhanced than double exchange, thus favoring antiferromagnetism. Compared to the  $Pnma$  case, the  $P4$  case has a larger effective hopping and the transition curve is shifted to favor antiferromagnetic ordering. This trend holds for both LSDA and LSDA+ $U$  calculations. Therefore, phenomenologically we can map  $Pnma$   $\text{La}_{1-x}\text{Sr}_x\text{MnO}_3$  to  $P4$   $\text{La}_{1-x}\text{Sr}_x\text{MnO}_3$  by choosing an appropriate Hubbard  $U$ . We find that in order to reproduce the ferromagnetic-to-antiferromagnetic transition around  $x \simeq 0.5$  in the  $P4$  case, we need  $3 \text{ eV} < U < 4 \text{ eV}$ . By comparison, to locate the correct transition point for  $Pnma$   $\text{La}_{1-x}\text{Sr}_x\text{MnO}_3$ ,  $U$  must be in the range of  $1 \text{ eV} < U < 2 \text{ eV}$  (see Fig. 2b).

## B. Choosing Hubbard $U$

The DFT+ $U$  approach is commonly used to study manganites [25]. However, neither the choice of Hubbard  $U$  value nor the method of choosing it is unanimous. Obviously, one can choose  $U$  based on purely empirical considerations that use experimental data: for example, we showed above that when  $1 \text{ eV} < U < 2 \text{ eV}$ , LSDA+ $U$  can correctly locate the experimental critical doping density ( $x = 0.5$ ) separating ferromagnetic and antiferromagnetic phases for bulk  $Pnma$  manganites. Below, we discuss two other reasonable-seeming methods one might consider to determine  $U$ . The approaches yield very different values of  $U$  that tend not to overlap and do not do well in comparison to experiment. In our opinion, unfortunately there is no reliable way to determine  $U$  in a theoretical *a priori* manner. Our opinion is that

a single-particle approach such as DFT+ $U$  will generally run into difficulties in describing strongly correlated system such as manganites, so that empiricism in choosing parameters is a necessary fact of life. Since the magnetic properties depend sensitively on the value of  $U$ , in our mind a more fruitful approach is to study a wide range of  $U$  to understand the trends versus  $U$  and especially *why* the trends take the form that they do instead of trying to make specific predictions based on some particular choice of  $U$ . (The  $U$  dependence of bulk manganite and ferroelectric/manganite interfaces are discussed in Sections III A 2 and IV C, respectively.)

### 1. Bulk $\text{LaMnO}_3$

First we may ask what  $U$  value properly describes the parent material: bulk  $\text{LaMnO}_3$ . This value then may be a reasonable guess for the doped manganites. Taking into account the structural distortions by using a  $c(2 \times 2) \times 2$  unit cell [25] and by relaxing all degrees of freedom, we calculate the total energies of different magnetic orderings and find their energy sequence as a function of  $U$ . The result is shown in Table II. In particular, we explicitly list  $\Delta E$ , defined by Eq. (1) in the table. We can see that within a wide range of  $U$ , the ground state is not the experimentally observed  $A$ -type antiferromagnet, nor is there any tendency that ferromagnetism could yield to antiferromagnetism in the large  $U$  limit. However, reproducing the insulating properties of the  $A$ -type antiferromagnetic phase requires  $U \geq 4$  eV.

We note that one can perform self-consistent calculations on bulk  $\text{LaMnO}_3$  using the experimental lattice parameters and atomic coordinates. It is possible to stabilize an insulating  $A$ -type ground-state for  $U \leq 1$  eV, as shown in Table III. For a comprehensive study of bulk  $\text{LaMnO}_3$  studied with a variety of exchange correlation functionals and basis sets, please refer to [33] and references therein. Unfortunately, the reproduction for the correct ground state when using experimental structures is not of great value for our study: we have a non bulk-like interfacial system where the in-plane lattice constants are fixed via epitaxy to a substrate and all remaining degrees of freedom must be relaxed, so we must return to Table II. It would seem the best choice is either  $U = 0$  (which stabilizes the incorrect ground-state by the least energy) or  $U > 4$  (which makes the  $A$ -type phase insulating). As shown above, neither choice is satisfactory in reproducing the experimental  $x \simeq 0.5$  phase

boundary for the doped manganites.

TABLE II: LSDA+ $U$  study of bulk  $\text{LaMnO}_3$ . The italic  $M$  means metallic and the italic  $I$  means insulating.  $F$  refers to ferromagnetic ordering.  $A$ ,  $C$  and  $G$  refer to  $A$ -type,  $C$ -type and  $G$ -type antiferromagnetic ordering, respectively [30].  $\Delta E$  is the energy difference between the ferromagnetic ordering and  $A$ -type antiferromagnetic ordering per Mn atom, defined by Eq. (1). The unit cell is orthorhombic. The experimental value of lattice constants is:  $a = 5.742 \text{ \AA}$ ,  $b = 7.668 \text{ \AA}$  and  $c = 5.532 \text{ \AA}$  [25]. The calculated lattice constants are for  $A$ -type antiferromagnetic ordering because the experimental ground state is  $A$ -type antiferromagnetic. In the parenthesis lists the relative difference between experimental and theoretical lattice constants.

$U$ (eV)	magnetic ordering	$\Delta E$ (meV)	$a(\text{\AA})$	$b(\text{\AA})$	$c(\text{\AA})$
0	$F(M) < A(M) < C(M) < G(M)$	40	5.402 (-5.9%)	7.468 (-2.6%)	5.458 (-1.3%)
2	$F(M) < A(M) < C(M) < G(I)$	61	5.567 (-3.0%)	7.560 (-1.4%)	5.435 (-1.8%)
4	$F(M) < A(I) < C(I) < G(I)$	65	5.644 (-1.7%)	7.584 (-1.1%)	5.448 (-1.5%)
6	$F(M) < A(I) < C(I) < G(I)$	76	5.699 (-0.8%)	7.624 (-0.6%)	5.465 (-1.2%)
8	$F(M) < A(I) < C(I) < G(I)$	98	5.743 (0.02%)	7.694 (0.3%)	5.482 (-0.9%)

## 2. Linear response approach of self-consistent $U$

Second, we may ask for a purely *ab initio* approach that delivers a value of  $U$  appropriate for the system within the framework of DFT+ $U$  itself. This is the linear response approach of Refs. [34, 35]. We focus on  $P4 \text{La}_{1-x}\text{Sr}_x\text{MnO}_3$  ( $x = 0.2$ ) as an example. We run a series of linear response calculations [34] on  $2 \times 2 \times 2$  unit cells of  $P4 \text{La}_{1-x}\text{Sr}_x\text{MnO}_3$ . The ground state is calculated using LSDA+ $U$  with a range of  $0 < U_{in} < 5 \text{ eV}$ . For each value of  $U_{in}$ , we use the extrapolation scheme in Ref. [34] to get the converged value of  $U_{out}$ . Then we collect all the converged  $U_{out}$  as a function of  $U_{in}$  and extract out  $U_{scf}$  [35] from the linear region. Our final value is  $U_{scf} = 5.8 \text{ eV}$ . As discussed above, to reproduce the experimental  $x \simeq 0.5$  boundary for  $P4 \text{La}_{1-x}\text{Sr}_x\text{MnO}_3$ , we require  $3 \text{ eV} < U < 4 \text{ eV}$ . The self-consistent  $U$  is significantly higher.

TABLE III: LSDA+ $U$  study of bulk LaMnO<sub>3</sub> using experimental coordinates and lattice constants. The italic  $M$  means metallic and the italic  $I$  means insulating.  $\Delta E$  is the energy difference between the ferromagnetic ordering and  $A$ -type antiferromagnetic ordering per Mn atom, defined by Eq. (1).

$U$ (eV)	magnetic ordering	$\Delta E$ (meV)
0	$A(I) < F(M)$	-15
1	$A(I) < F(M)$	-4
2	$F(M) < A(I)$	4
3	$F(M) < A(I)$	10
4	$F(M) < A(I)$	17

#### IV. FERROELECTRIC/MANGANITE INTERFACES

##### A. Methodology

Our computational supercell for interface calculations is schematically illustrated in Fig. 3. The  $x$  and  $y$  directions of the simulation cell are subject to periodic boundary conditions and their lengths are fixed to our computed theoretical lattice constant of SrTiO<sub>3</sub>  $a = 3.85 \text{ \AA}$  (1.5% smaller than the experimental value), because in experiments La<sub>1-x</sub>Sr<sub>x</sub>MnO<sub>3</sub> is epitaxially grown on a SrTiO<sub>3</sub> substrate [13]. In order to directly compare to the experiment, all the results shown below are from calculations with the nominal doping level chosen as  $x = 0.2$  (unless otherwise specified). In addition to PbTiO<sub>3</sub> and La<sub>1-x</sub>Sr<sub>x</sub>MnO<sub>3</sub>, we also include the electrode Pt to provide an electron reservoir and  $\simeq 20 \text{ \AA}$  vacuum to separate periodic copies of the slabs. We strain the in-plane lattice constant of the entire slab structure to that of bulk SrTiO<sub>3</sub> to impose the epitaxial strain from the substrate. In the simulation cell (Fig. 3) and in most of our calculations, we do not include a SrTiO<sub>3</sub> substrate explicitly in order to keep the computations from becoming unwieldy in scale. However, in Appendix B we present a few calculations that do include the SrTiO<sub>3</sub> substrate explicitly, and it is shown that the interfacial structural and magnetic properties between PbTiO<sub>3</sub>/La<sub>1-x</sub>Sr<sub>x</sub>MnO<sub>3</sub> are well converged when the La<sub>1-x</sub>Sr<sub>x</sub>MnO<sub>3</sub> film is 4 unit cells or thicker. In addition to reducing the computational burden, the absence of a SrTiO<sub>3</sub> substrate creates a manganite surface that allows us to apply a hole counting method which

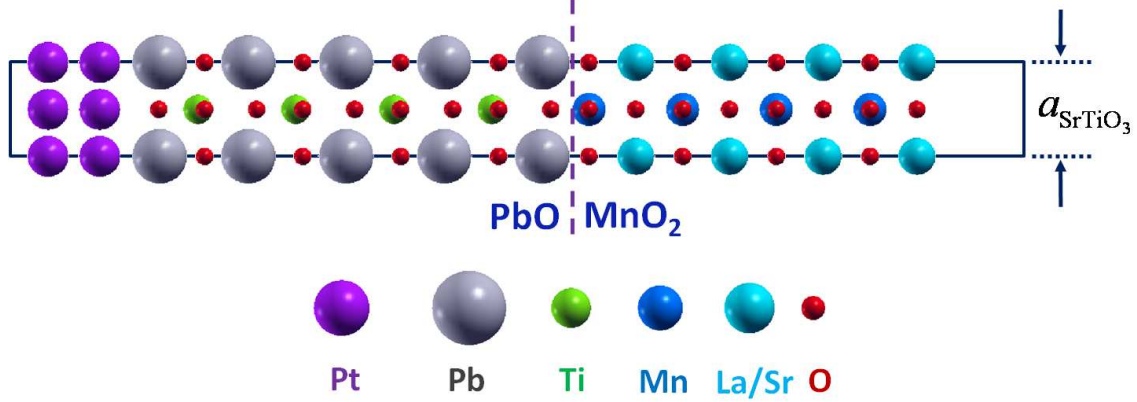


FIG. 3: (Color online) Illustration of the computational supercell. The dashed line highlights the PbO/MnO<sub>2</sub> interface. The whole structure is coherently strained to the lattice constant of SrTiO<sub>3</sub>. Vacuum  $\simeq 20$  Å thick is introduced to separate periodic copies. An XO ( $X=\text{La/Sr}$ ) atomic layer faces the vacuum.

can much more accurately calculate the hole spatial distribution than the use of Löwdin orbitals [16] (see Appendix C for details). Since the SrTiO<sub>3</sub> substrate is typically TiO<sub>2</sub>-terminated and the manganites are in principle deposited stoichiometrically and epitaxially on the SrTiO<sub>3</sub>, the resulting ferroelectric/manganite interface is taken to be PbO/MnO<sub>2</sub>.

Using the Berry phase method [36], we find that SrTiO<sub>3</sub>-strained PbTiO<sub>3</sub> has bulk polarization 0.74 C/m<sup>2</sup>. For the two different directions of ferroelectric polarization, we define two distinct states: the accumulation state in which extra holes are induced into the interfacial La<sub>1-x</sub>Sr<sub>x</sub>MnO<sub>3</sub> and depletion state in which extra electrons are induced into the interfacial La<sub>1-x</sub>Sr<sub>x</sub>MnO<sub>3</sub> (i.e., holes are driven out). One unit cell of PbTiO<sub>3</sub> in the interior is fixed to the bulk ferroelectric PbTiO<sub>3</sub> positions, an choice that simulates the behavior of a thick PbTiO<sub>3</sub> film. All remaining atomic coordinates in the slab are relaxed. We need to mention that our choice of boundary condition on ferroelectrics is consistent with the experiment [13] in which a thick film of 250 nm Pb(Zr<sub>0.2</sub>Ti<sub>0.8</sub>)O<sub>3</sub> is deposited on La<sub>1-x</sub>Sr<sub>x</sub>MnO<sub>3</sub>. However, the boundary condition on the ferroelectric could be different, depending on the experiments to be studied. For example, in Ref. [15], three unit cells of BaTiO<sub>3</sub> adjacent to a La<sub>0.7</sub>Sr<sub>0.3</sub>MnO<sub>3</sub> film are fully relaxed without the presence of Pt electron reservoir, in order to simulate the ultra-thin ferroelectrics used in other experiments [14]. Interestingly, the results of magnetoelectric coupling in Ref. [15] are consistent with ours, described below.

In Fig. 4, we show the cation-oxygen  $z$ -axis displacements of a representative PbTiO<sub>3</sub>

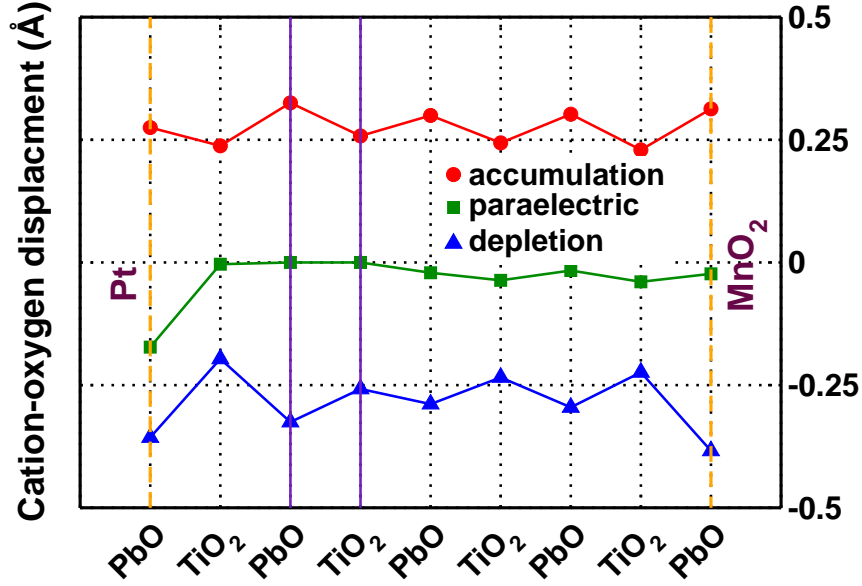


FIG. 4: (Color online) Cation-oxygen displacements along  $z$ -axis for the  $\text{PbTiO}_3$  film inside the  $\text{Pt}/\text{PbTiO}_3/\text{La}_{1-x}\text{Sr}_x\text{MnO}_3$  heterostructures. The two purple solid lines highlights the one unit cell of  $\text{PbTiO}_3$  that is fixed to bulk positions. The two orange dashed lines show the interfaces: left is the one facing Pt electrodes and right is the one that faces  $\text{La}_{1-x}\text{Sr}_x\text{MnO}_3$ .

thin film within the slab structure. The single fixed unit cell is highlighted by the two solid purple lines. The two interfaces (one faces  $\text{La}_{1-x}\text{Sr}_x\text{MnO}_3$  and the other faces Pt electrodes) are shown by the orange dashed lines. The sign of the displacements indicates polarization directions. We can see that in the relaxed  $\text{PbTiO}_3$ , there is no reversal of ferroelectric polarization and the magnitude of polarization is homogeneous. In addition, we also calculate an artificial state in which one unit cell of  $\text{PbTiO}_3$  is fixed to be paraelectric (i.e., zero cation-oxygen rumpling in the (100) atomic plane of the fixed unit cell).

Finally, we mention that most of the results presented below are calculated for an in-plane  $c(2 \times 2)$  unit cell which is compatible with the structural distortions found in bulk  $Pnma$   $\text{La}_{1-x}\text{Sr}_x\text{MnO}_3$ . Such calculations are referred to as  $c(2 \times 2)$   $\text{La}_{1-x}\text{Sr}_x\text{MnO}_3$  interface calculations. In order to converge the hole distribution versus  $\text{La}_{1-x}\text{Sr}_x\text{MnO}_3$  thickness without inordinately increasing the computational burden, we increase the thickness of manganites by reducing the in-plane cell to  $1 \times 1$ . Those calculations are referred to as  $1 \times 1$   $\text{La}_{1-x}\text{Sr}_x\text{MnO}_3$  interface calculations.

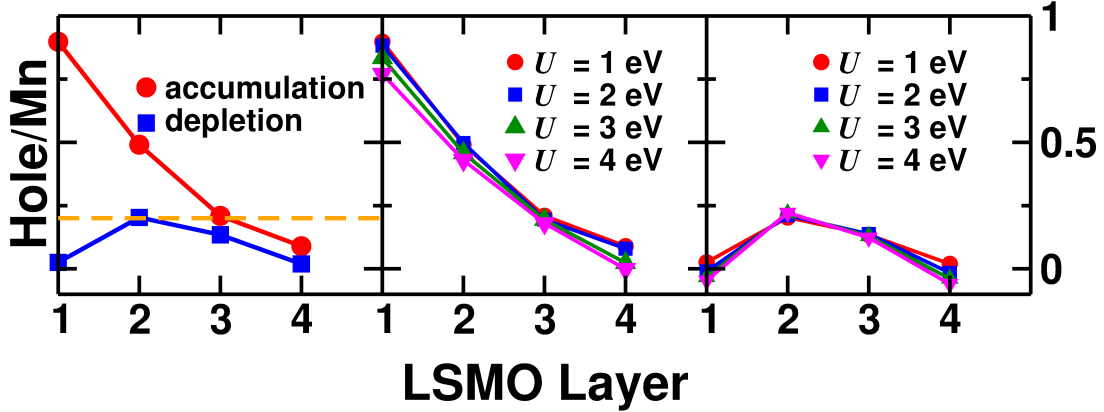


FIG. 5: (Color online) Left panel: hole distributions of the accumulation and depletion states of  $c(2 \times 2)$   $\text{La}_{1-x}\text{Sr}_x\text{MnO}_3$  ( $U = 1$  eV). Middle panel: Hubbard  $U$  dependence of hole distribution in the accumulation state. Right panel: Hubbard  $U$  dependence of hole distribution in the depletion state.

## B. Charge modulation

We first study the effect of charge modulation from switching the ferroelectric polarization of  $\text{PbTiO}_3$ . In the presence of ferroelectric  $\text{PbTiO}_3$ , the charge density of  $\text{La}_{1-x}\text{Sr}_x\text{MnO}_3$  at the interface differs from its bulk value because the polarization of  $\text{PbTiO}_3$  terminates at the interface and results in the surface charge (the surface charge density is  $\sigma = \mathbf{P} \cdot \mathbf{n} = P_z$ ). Since  $\text{La}_{1-x}\text{Sr}_x\text{MnO}_3$  is metallic, this surface charge induces screening charge in the  $\text{La}_{1-x}\text{Sr}_x\text{MnO}_3$  equal in magnitude but opposite in sign to the surface charge. When the  $\text{PbTiO}_3$  switches its polarization, the surface charge changes sign and so does the screening charge. Therefore a net change of charge density ( $\Delta\sigma = 2P_z$ ) is induced in the  $\text{La}_{1-x}\text{Sr}_x\text{MnO}_3$  thin film.

The left panel of Fig. 5 shows the hole distribution of a 4 unit cells thick  $\text{La}_{1-x}\text{Sr}_x\text{MnO}_3$  film on  $\text{PbTiO}_3$ . The method of counting holes is described in the Appendix C. The nominal doping is  $x = 0.2$ , highlighted by the dashed line. This calculation is performed on  $c(2 \times 2)$   $\text{La}_{1-x}\text{Sr}_x\text{MnO}_3$  with  $\text{LSDA}+U$  ( $U = 1$  eV). The  $\text{PbO}/\text{MnO}_2$  interface is at layer 1, and layer 4 is the artificial surface. As expected, the hole distribution accumulates (depletes) at the interface when the surface charge is negative (positive).

The middle and right panel of Fig. 5 show the Hubbard  $U$  dependence of spatial hole distribution for the accumulation and depletion states, respectively. The calculation is per-



formed on the same structure as in the left panel of Fig. 5. Since the induced holes (or electrons) extend into the  $\text{La}_{1-x}\text{Sr}_x\text{MnO}_3$  within the screening length (which does not strongly depend on the correlation), it is not surprising that Hubbard  $U$  does not significantly change the hole distribution. As a good approximation, we assume that the hole distribution does not depend on Hubbard  $U$ .

In order to get a spatial distribution of holes that is well converged with the manganite thickness, we run a calculation with 8 unit cells of  $1 \times 1 \text{ La}_{1-x}\text{Sr}_x\text{MnO}_3$ . This calculation is performed with LSDA+ $U$  ( $U=4$  eV). The results are shown in Fig. 6. From Fig. 6a, the screening length of the accumulation state is estimated to be 3 unit cells while the screening length of depletion state seems to be only 1 unit cell. The asymmetry is due to the fact that there are two factors affecting the hole distribution. One is the induced screening charge and the other is the presence of PbO/MnO<sub>2</sub> interface itself. To demonstrate the role of the interface, we perform a test calculation in which the PbTiO<sub>3</sub> thin film is forced to be paraelectric and find (see the orange triangle symbols in Fig. 6a) that the resulting hole distribution is not uniform nor equal to the nominal doping ( $x = 0.2$ ) at the interface. This non-uniform hole distribution can be considered as a background, owing to the chemistry of the PbO/MnO<sub>2</sub> interface. If we subtract the hole distributions of accumulation and depletion states from this background, we can see that the “net” hole distributions of accumulation and depletion states now become more symmetric, with the screening length of depletion state a little larger than that of accumulation state (Fig. 6b). This is consistent with the Thomas-Fermi picture that depletion states have less carriers (holes) and therefore a larger screening length. To further verify this Thomas-Fermi picture, we perform the same calculation with a layer nominal hole doping  $x = 0.5$  and find very similar results (see Fig. 6c and d).

### C. Magnetization modulation

In this section, we study in detail whether the charge modulation can induce a spin modified configuration in the ground state. This means that the change of the magnetization is not simply proportional to that of the charge density (i.e. simple filling/emptying of Mn orbitals with fixed spin polarization) but involves a more dramatic change of magnetic structure at the interface. The mechanism is as follows: in the accumulation state, the

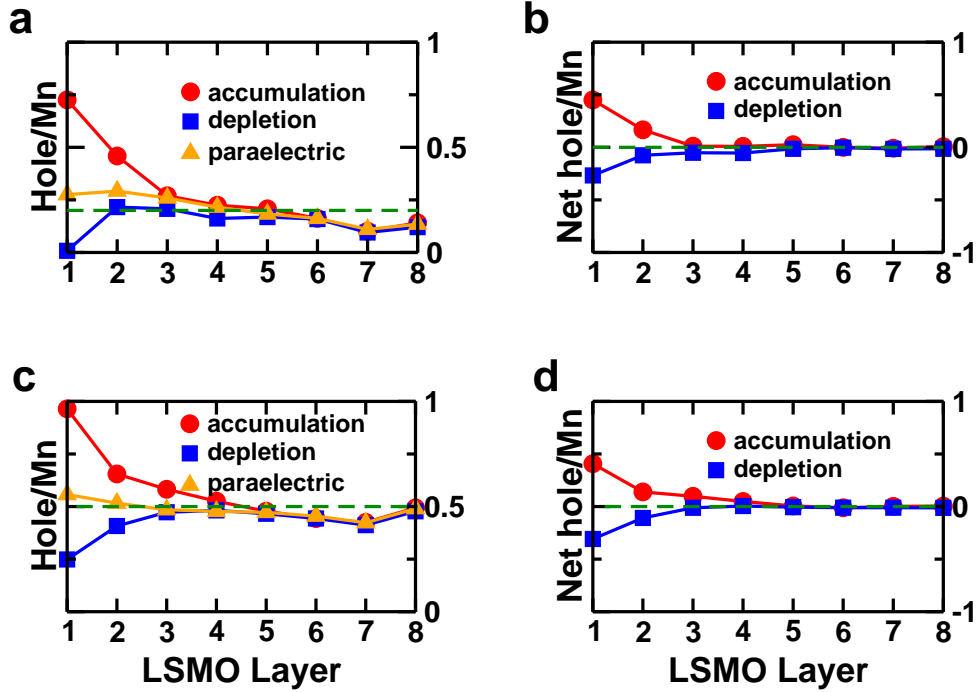


FIG. 6: (Color online) **a)** Hole distributions of  $1 \times 1$   $\text{La}_{1-x}\text{Sr}_x\text{MnO}_3$  8 unit cells thick with  $x = 0.2$  ( $U = 4$  eV). In addition to accumulation and depletion states, a test calculation in which  $\text{PbTiO}_3$  is fixed to be paraelectric is done and the resulting hole distribution is shown with orange triangles. **b)** “Net” hole distributions of  $1 \times 1$   $\text{La}_{1-x}\text{Sr}_x\text{MnO}_3$  8 unit cells thick with  $x = 0.2$  ( $U = 4$  eV): the paraelectric state background (see **a**)) is subtracted from the hole distributions of accumulation and depletion states. **c)** Hole distributions of  $1 \times 1$   $\text{La}_{1-x}\text{Sr}_x\text{MnO}_3$  8 unit cells thick with  $x = 0.5$  ( $U = 4$  eV). **d)** “Net” hole distributions in  $1 \times 1$   $\text{La}_{1-x}\text{Sr}_x\text{MnO}_3$  8 unit cells thick with  $x = 0.5$  ( $U = 4$  eV).

local hole distribution adjacent to the interface could be higher than  $x = 0.5$ , the critical value for the ferro-to-antiferromagnetic transition. Therefore the spins at the interfacial region could flip. However, in the depletion state, such a local spin-flip is not expected to occur. Therefore from now on, we only focus on the accumulations state. In order to study whether this local phase transition does occur at the interface by switching the polarization, we consider three relevant spin configurations ( $F$ ,  $A1$  and  $A2$ ), illustrated in Fig 7. When all the spins are ferromagnetically coupled, this configuration is denoted as  $F$  (Fig. 7a). If

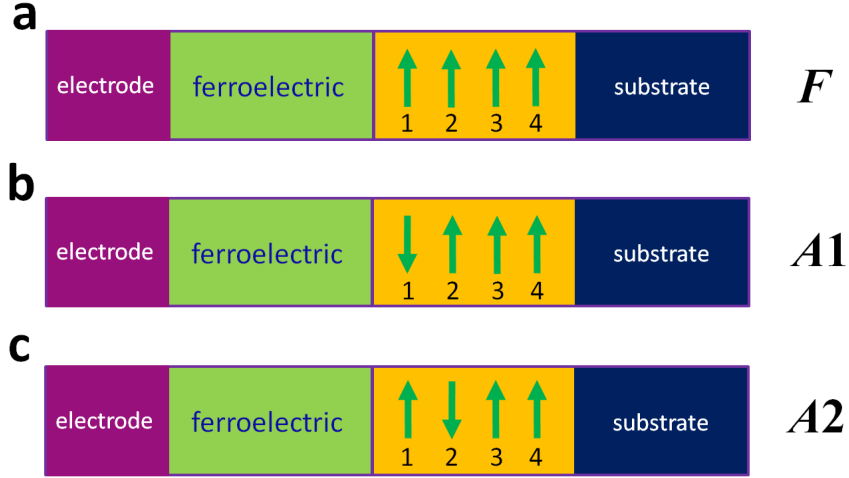


FIG. 7: (Color online) Illustration of different magnetic structures. **a)** Ferromagnetic configuration, denoted by  $F$ . **b)** Spin flips in the first unit cell, denoted by  $A1$ . **c)** Spin flips in the second unit cell, denoted by  $A2$ .

the spin is flipped in the first unit cell of manganite from the interface, this configuration is denoted by  $A1$  (Fig. 7b). Finally, if the spin is flipped in the second unit cell of manganite, then we denote it by  $A2$  (Fig. 7c). We address three important and related questions below: i) whether the ground-state magnetic structure depends on  $U$ ? ii) given a reasonable  $U$ , whether the manganite nominal doping  $x$  could change the final magnetic structure? iii) how the structural distortions at the interface may affect the magnetic structures?

### 1. Hubbard $U$ dependence

We obtain the total energies of these three spin configurations with a range of Hubbard  $U$  and collect all the results in Fig. 8. We use the following definitions of energy differences:

$$\Delta E_1 = E(A1) - E(F) \quad (2)$$

$$\Delta E_2 = E(A2) - E(F) \quad (3)$$

From Fig. 8 we can see that the magnetic structure of the ground state evolves with Hubbard  $U$ . When  $U$  is small ( $U < 0.9$  eV), the ground state has the magnetic structure of  $A2$ . With  $U$  increasing ( $0.9$  eV  $< U < 2.4$  eV), the ground state evolves into  $A1$ . When  $U$  gets even

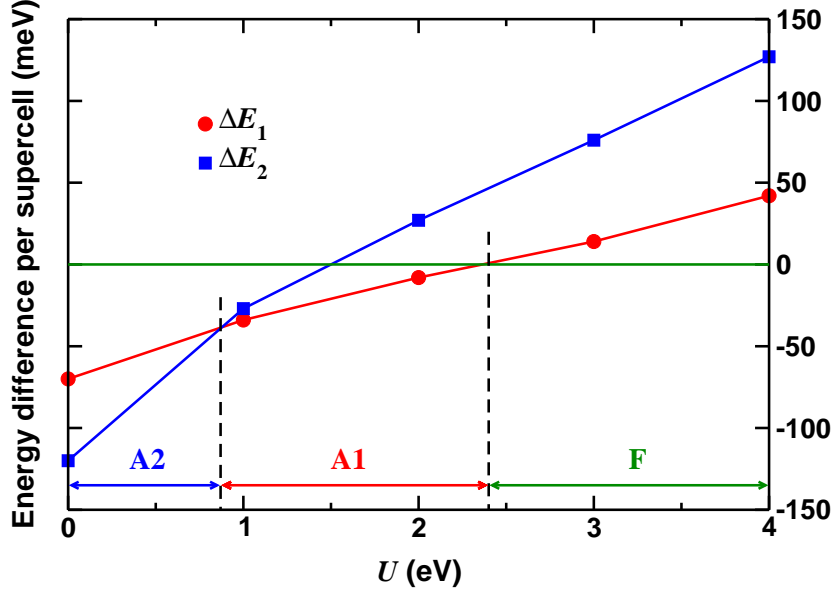


FIG. 8: (Color online) Energy sequence dependence on Hubbard  $U$ .  $\Delta E_1 = E(A1) - E(F)$  and  $\Delta E_2 = E(A2) - E(F)$ . The labels ( $F$ ,  $A1$  and  $A2$ ) show the ground state in different regions of Hubbard  $U$ . The boundary between  $F$  and  $A1$  is 2.4 eV and that between  $A1$  and  $A2$  is 0.9 eV.

larger ( $U > 2.4$  eV), we have  $F$  as the ground state. Therefore any prediction of the magnetic properties of the interface depends greatly on the choice of  $U$ . Before we pick a reasonable value of  $U$ , we need to understand why the magnetic structure is so sensitive to the Hubbard  $U$ . The answer is that  $U$  changes the bulk phase transition point so that for the same hole distribution, the preferred local magnetic phase also changes. We can see from Fig. 8 that increasing the Hubbard  $U$  drives the local phase at the interface from antiferromagnetic to ferromagnetic, which is consistent with the  $U$  dependence in the bulk (see Fig. 2b). In order to more quantitatively describe the energy sequence, we construct an Ising-like model which is based on the interaction between nearest neighbor Mn magnetic moments [39]:

$$E = - \sum_{\langle ij \rangle} J_{ij} m_i m_j \quad (4)$$

where  $\langle ij \rangle$  range is over all nearest neighbors and  $m_i$  is the magnetization in each  $\text{MnO}_2$  layer of the manganites. The labelling of manganite layers is shown in Fig. 7. We assume that the hole spatial distribution does not sensitively depend on magnetic structures [40], and obtain:

$$\Delta E_1 = 2J_{12}|m_1m_2| \quad (5)$$

$$\Delta E_2 = 2J_{12}|m_1m_2| + 2J_{23}|m_2m_3| \quad (6)$$

In order to get an energy sequence, we need to know the signs of  $J_{12}$  and  $J_{23}$ . From the bulk calculations, at a given hole doping  $x$  and assuming half-metallicity, the magnetization is related to the hole doping  $x$  by  $m = (4 - x)\mu_B$  where  $\mu_B$  is the Bohr magneton. The exchange coupling  $J$  can be extracted out by:

$$J = \frac{E(A) - E(F)}{2m^2} \quad (7)$$

where the energy difference  $\Delta E = E(A) - E(F)$  is from the bulk calculations, shown in Fig. 2.  $J$  changes sign at the transition point. From Eq. (7),  $J$  is positive for ferromagnetic phase and negative for  $A$ -type antiferromagnetic phase. At the interface, however, the hole spatial distribution is not uniform (see Fig. 6). We assume that the interface coupling  $J_{ij}$  is that of bulk  $\text{La}_{1-x}\text{Sr}_x\text{MnO}_3$  but for a doping value that is the average of the neighboring layers  $i$  and  $j$ :

$$J_{ij} \simeq J_{\text{bulk}} \left( \frac{x_i + x_j}{2} \right) \quad (8)$$

We need a final good approximation, which is verified in Fig. 5, that the hole distribution does not sensitively depend on Hubbard  $U$ . Based on Eq. (5-8), we start with a large Hubbard  $U$ . Since large  $U$  favors ferromagnetism (see Fig. 2b), the bulk phase is ferromagnetic and both  $J_{12}$  and  $J_{23}$  are positive. Thus  $0 < \Delta E_1 < \Delta E_2$  and we have the following energy sequence:  $F < A1 < A2$ . We denote this by case 1. With a decreasing  $U$ , the transition point is moved to smaller hole doping region. Noting that the hole distribution monotonically decays from the interface (see Fig. 6), we always have  $(x_1 + x_2)/2 > (x_2 + x_3)/2$ . Hence  $J_{12}$  changes sign earlier than  $J_{23}$  as  $U$  decreases. If  $U$  is in such a range that  $J_{12}$  just becomes negative but  $J_{23} > 0$ , we have  $\Delta E_1 < 0$  and  $\Delta E_2 > 0$ . The energy sequence is now  $A1 < F < A2$ , which is denoted by case 2. As  $U$  further decreases, so that  $J_{12}$  becomes very negative and  $J_{23}$  remains positive but  $J_{12}|m_1| + J_{23}|m_3| < 0$ , then we have  $\Delta E_1 < \Delta E_2 < 0$ . The energy sequence becomes  $A1 < A2 < F$ . This is case 3. With  $U$  further decreasing, the bulk phase becomes always antiferromagnetic, both  $J_{12}$  and  $J_{23}$  become negative, and we

TABLE IV: The energy sequence predicted from the simple model and the comparison with the DFT calculations with different Hubbard  $U$ .

model		DFT		
case	energy sequence	$U$ (eV)	$\Delta E_1$ (meV)	$\Delta E_2$ (meV)
1	$0 < \Delta E_1 < \Delta E_2$	3	14	76
2	$\Delta E_1 < 0 < \Delta E_2$	2	-8	27
3	$\Delta E_1 < \Delta E_2 < 0$	1	-34	-27
4	$\Delta E_2 < \Delta E_1 < 0$	0	-70	-120

have  $\Delta E_2 < \Delta E_1 < 0$ . The final possible energy sequence is  $A2 < A1 < F$ , which is denoted by case 4. These four energy sequences exhaust all the possibilities and are summarized in Table IV. Now we compare the DFT results (see Fig. 8) to the energy sequence predicted from the model (see Table IV). As the Hubbard  $U$  evolves from 0 to 4 eV, we find all four cases. For example,  $U = 3$  eV corresponds to  $F < A1 < A2$ ;  $U = 2$  eV to  $A1 < F < A2$ ;  $U = 1$  eV to  $A1 < A2 < F$  and  $U = 0$  eV to  $A2 < A1 < F$ . The exact boundaries of Hubbard  $U$  for each energy sequence can be found in Fig. 8.

Since the Hubbard  $U$  changes the transition point and the magnetic structure of the ground state of the  $\text{PbTiO}_3/\text{La}_{1-x}\text{Sr}_x\text{MnO}_3$  interface, we need to determine what is the reasonable value of  $U$ . Following Ref. [12], we argue that because the magnetic structures sensitively depend on the transition point, we need to choose a range of  $U$  so that the ferromagnetic-to-antiferromagnetic transition occurs around  $x \simeq 0.5$ . From bulk calculations, we know that as  $1 \text{ eV} < U < 2 \text{ eV}$  for  $Pnma$   $\text{La}_{1-x}\text{Sr}_x\text{MnO}_3$ , this criterion is satisfied. On the other hand, when  $U$  is in this range, the magnetic structure of the ground state is always  $A1$ . Therefore by switching the  $\text{PbTiO}_3$  polarization, we do find a spin-modified configuration in the DFT simulation, provided that our choice of  $U$  is reasonable. This prediction is consistent with the recent experiment [13] which observes an anomalously large change in the magnetization as the polarization of ferroelectrics is switched and which assigns this to a spin-flip on the Mn atom closest to the interface.

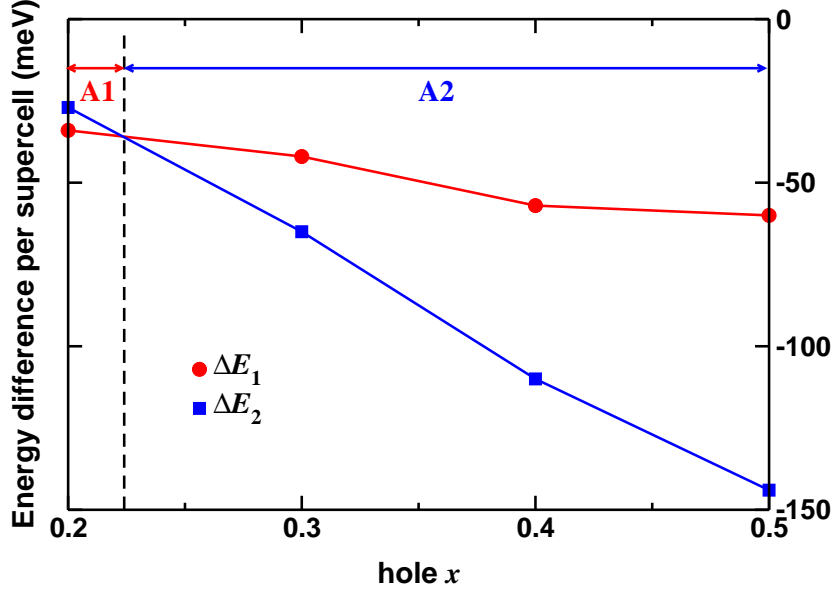


FIG. 9: (Color online) Energy dependences of the interfacial magnetic states as a function of the doping  $x$  of the  $\text{La}_{1-x}\text{Sr}_x\text{MnO}_3$ .  $\Delta E_1 = E(A1) - E(F)$  and  $\Delta E_2 = E(A2) - E(F)$ . The boundary between the phases is at  $x_c \approx 0.22$  denoted by the vertical dashed line.  $A1$  is stable to the left and  $A2$  to the right of the boundary. The results are based on LSDA+ $U$  with  $U = 1$  eV.

## 2. Hole dependence

The ground-state magnetic structure we found above ( $A1$  configuration) is consistent with the experimental conjecture, but it is different from the  $A2$  configuration found using DFT+GGA for the similar multiferroelectric structure  $\text{BaTiO}_3/\text{La}_{1-x}\text{Ba}_x\text{MnO}_3$  with  $x = 0.5$  [12]. We find that the reason for the differing ground state magnetic structure is due to the doping  $x$  dependence of the system. Specifically, for  $U = 1$  eV, we calculate the energies of the  $A1$  and  $A2$  interfacial states versus doping  $x$  and present the results in Fig. 9.

When the nominal doping  $x$  is near the bulk magnetic transition point  $x = 0.5$ , the Fig. 9 shows that the ground state should be  $A2$  which is consistent with Ref. [12]. However, the actual experimental doping  $x = 0.2$  is far below  $x = 0.5$ , the ground state should be  $A1$ . We calculate the phase boundary between  $A1$  and  $A2$  to be  $x_c \approx 0.22$  for  $U = 1$  eV. This transition from  $A1$  to  $A2$  is easily understood in the framework of our Ising-like model. Each pair of neighboring Mn magnetic moments could be either ferromagnetically or

antiferromagnetically coupled depending on the number of holes on the pair of Mn atoms. When the doping  $x$  is low, the ferroelectric modulation of the hole density must drop to a low value within a few unit cells from the interface (see Fig. 6) and thus only the first two moments  $(m_1, m_2)$  will be paired antiferromagnetically, which leads to  $A1$ . However, when the doping  $x$  is high, the larger values of the hole density means that both the  $(m_1, m_2)$  and  $(m_2, m_3)$  pairs couple antiferromagnetically, which leads to  $A2$ . As a final remark, we note that our Ising-like model predicts that the transition doping  $x_c$  between  $A1$  and  $A2$  should depend on Hubbard  $U$ : since increasing  $U$  favors ferromagnetism, larger  $U$  will increase  $x_c$  (i.e, require more holes for antiferromagnetism).

### 3. Structural distortion dependence

Due to the presence of ferroelectric polarization, significant distortions that deviate from bulk manganites are observed in the relaxed ground state structures. Concerning each oxygen octahedron that encloses Mn atoms, we calculate  $c/a$  ratio and rumpings  $\delta/a$  in each  $\text{MnO}_2$  layer, where  $c$  is the distance between the two apical oxygen atoms along the  $z$  direction,  $\delta$  is the vertical displacement between Mn and O, and  $a$  is the lattice constant of  $\text{SrTiO}_3$  substrate. The results are summarized in Table V. Since the spin-flipped process occurs at the interface in the accumulation state, we only show  $c/a$  ratio and  $\delta/a$  of the first and second manganite layers from the interface, and from now on the discussion is constrained to the accumulation state. From Table V, we can see that in the accumulation state, there are significant polar distortions at the interface ( $\delta/a$  is as large as 6%). It was shown in Ref. [12] that the spin-flipped process is mainly of electronic origin rather than due to the polar distortions at the interface. In this section, we use detailed comparisons to show that though the spin-modified configuration is due to electronic reconstructions, polar distortions need to be taken into account in order to make a quantitative (instead of qualitative) link between the interface phase and bulk phases.

Now we look at the Ising-like model Eq. (5-8) more closely. The model is based on the assumption that the local magnetic structure can be predicted from bulk manganites of the same hole doping. In Table VI, we list the energy difference between  $F$  and  $A1$  interfacial configurations from the interface calculations, defined by



TABLE V: The  $c/a$  ratio of each oxygen octahedron that encloses Mn atoms and rumplings  $\delta/a$  of each  $\text{MnO}_2$  layer for both accumulation and depletion states.  $c$  is the distance between the two apical oxygen atoms along the  $z$  direction.  $\delta$  is the rumplings of  $\text{MnO}_2$  layer, and  $a$  is the lattice constant of  $\text{SrTiO}_3$  substrate. Layer1 and layer2 refer to the first and second unit cell of manganites from the interface.

accumulation state			depletion state		
	layer1	layer2		layer1	layer2
$c/a$	0.97	0.94	$c/a$	1.05	0.98
$\delta/a$	0.06	0.02	$\delta/a$	0.01	0.001

$$\Delta E_I = E(A1) - E(F) \quad (9)$$

where  $E(F)$  and  $E(A1)$  are the total energies of  $F$  and  $A1$  configurations, respectively. We also calculate the average hole density between the first and second layers, i.e.  $\bar{x} = (x_1 + x_2)/2$ . Next, we list the *bulk* energy difference  $\Delta E_B$ , defined as

$$\Delta E_B = \frac{1}{2} (E_B(A) - E_B(F)) \quad (10)$$

where  $E_B(F)$  and  $E_B(A)$  are the total energies of  $\text{SrTiO}_3$ -strained  $\text{La}_{1-x}\text{Sr}_x\text{MnO}_3$  with ferromagnetic and  $A$ -type antiferromagnetic ordering, respectively. The factor  $\frac{1}{2}$  is included because in the bulk form wherever a Mn atom flips its spin, there are two Mn-Mn bonds involved owing to periodic boundary conditions, whereas at the interface a Mn spin flip only involves one Mn-Mn bond. Hence, we need a factor  $\frac{1}{2}$  so that both  $\Delta E_I$  and  $\Delta E_B$  describe the energy difference *per* Mn-Mn bond. The nominal hole doping  $x$  is chosen as the same as  $\bar{x}$  from the supercell calculations. Table VI shows that although the trend versus  $U$  is the same in both supercell and bulk calculations, the magnitudes of  $\Delta E$  do not agree at all. There must be something at the interface which is absent in bulk phase and significantly affects the energy difference between antiferro- and ferromagnetism.

We find that, due to the presence of ferroelectric  $\text{PbTiO}_3$ , strong polar distortions are induced at the interface layer of  $\text{MnO}_2$  in the accumulation state (Table V), as is illus-

TABLE VI: The comparison of energy difference between the interface calculations and bulk  $\text{La}_{1-x}\text{Sr}_x\text{MnO}_3$  calculations.  $\bar{x} = (x_1 + x_2)/2$  is the average hole in the first and second  $\text{La}_{1-x}\text{Sr}_x\text{MnO}_3$  layers closest to the interface. For different Hubbard  $U$ ,  $\bar{x}$  does not change significantly.  $\Delta E_I$  is the energy difference between phases  $A1$  and  $F$  from the supercell calculations.  $\Delta E_B$  is the energy difference of  $\text{SrTiO}_3$ -strained *bulk*  $\text{La}_{1-x}\text{Sr}_x\text{MnO}_3$  between  $A$ -type antiferromagnetism ( $A$ ) and ferromagnetism ( $F$ ).  $\Delta E_{BP}$  is the energy difference between  $E(A)$  and  $E(F)$  of  $\text{SrTiO}_3$ -strained *bulk*  $\text{La}_{1-x}\text{Sr}_x\text{MnO}_3$ , with the interfacial polar distortions manually included and  $c$ -axis optimized. For bulk calculations ( $\Delta E_B$  and  $\Delta E_{BP}$ ), the nominal hole density is chosen as  $\bar{x}$ .

$U$ (eV)	$\bar{x}$	$\Delta E_I$ (meV)	$\Delta E_B$ (meV)	$\Delta E_{BP}$ (meV)
1	0.7	-34	-112	-47
2	0.7	-8	-70	-17
3	0.65	14	-24	16
4	0.6	42	19	57

trated in Fig. 10a. The cation-oxygen vertical displacement in  $\text{MnO}_2$  at the interface is  $\delta = 0.2 \text{ \AA}$ . Such a strong polar distortion (distinguished from the structural distortions of  $Pnma$  symmetry) is absent in bulk  $\text{La}_{1-x}\text{Sr}_x\text{MnO}_3$  and is a direct consequence of the ferroelectric/manganite interface. In order to show explicitly how this interfacial polar distortion affects the energy difference between  $F$  and  $A$ -type magnetic orderings, we perform the following thought experiment, which is schematically illustrated in Fig. 10b. We focus on the two layers of  $\text{La}_{1-x}\text{Sr}_x\text{MnO}_3$  closest to the interface in interface calculations, use their relaxed atomic positions and choose an  $x$  that is equal to the average hole doping  $\bar{x} = (x_1 + x_2)/2$  from interface calculations. In this way, we create such artificial  $\text{La}_{1-\bar{x}}\text{Sr}_{\bar{x}}\text{MnO}_3$  with the same built-in polar distortions and the same average hole doping as the two manganite layers at the interface. We impose periodic boundary conditions on this artificial  $\text{La}_{1-\bar{x}}\text{Sr}_{\bar{x}}\text{MnO}_3$ , fix all atom positions and in-plane lattice constants, and optimize the  $c$ -axis to minimize the out-of-plane stress. We tune  $c$  separately for both ferromagnetism and  $A$ -type antiferromagnetism. A similar energy difference  $\Delta E_{BP}$  (subscript  $P$  means ‘polarized’) is defined as

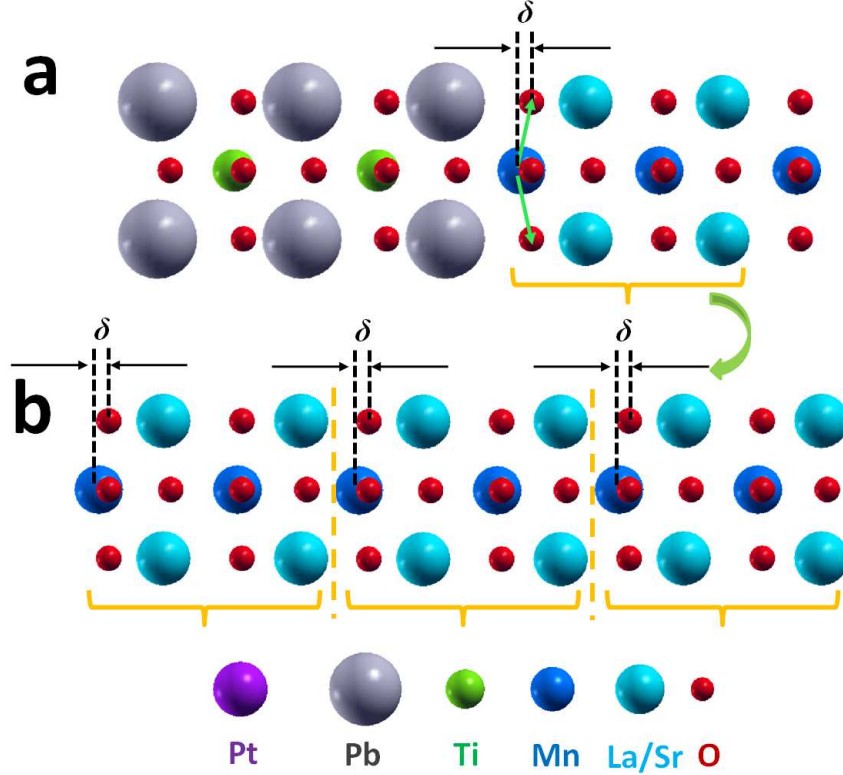


FIG. 10: (Color online) **a**) Strong polar distortion is induced at the interface layer of  $\text{MnO}_2$  due to the presence of  $\text{PbTiO}_3$ . **b**) Schematics of copying the two interfacial  $\text{La}_{1-x}\text{Sr}_x\text{MnO}_3$  layers and forming artificial bulk  $\text{La}_{1-x}\text{Sr}_x\text{MnO}_3$  with built-in polar distortions.

$$\Delta E_{BP} = \frac{1}{2} (E_{BP}(A) - E_{BP}(F)) \quad (11)$$

where  $E_{BP}(F)$  and  $E_{BP}(A)$  are the total energies of the artificially constructed  $\text{La}_{1-x}\text{Sr}_x\text{MnO}_3$  with ferromagnetic and  $A$ -type antiferromagnetic ordering, respectively. We can see from Table VI that  $\Delta E_{BP}$  is much closer to  $\Delta E_I$  than the raw bulk data  $\Delta E_B$ , demonstrating that in order to quantitatively connect the phase evolution of the ferroelectric/manganite interface from the bulk manganite phases, the polar distortion induced in interfacial manganites is an essential ingredient in modelling.

## V. CONCLUSION

We have presented a systemic study of the  $\text{PbTiO}_3/\text{La}_{1-x}\text{Sr}_x\text{MnO}_3$  interface as a prototype for ferroelectric/manganite interfaces. We are able to show that the screening charges

produced in the manganite in response to the ferroelectric surface charge are sufficient to change the magnetic state of the interfacial manganite from ferromagnetic to antiferromagnetic, in agreement with experimental observations and interpretations. In the process, we have developed a method to accurately count the layer-by-layer hole distribution in the manganite thin film which allows us to perform quantitative analysis of the system. For example, it allows us to create a simple Ising-like model of the interfacial magnetism that uses bulk parameters to reproduce the computed behaviors.

One of main theoretical findings is that the ground-state magnetic state depends sensitively on the value of  $U$  chosen in the LSDA+ $U$  computation. We show that different reasonable-seeming approaches to determining  $U$ , and in particular some that are *ab initio* and deliver a  $U$  value appropriate to LSDA+ $U$  self-consistently, yield significantly different  $U$  values. Not all the values do well when compared to experiment. By asking that the LSDA+ $U$  calculation should correctly reproduce the critical hole doping density separating the ferromagnetic and antiferromagnetic phases, we are able to find a narrow range of  $U$  values that also produce a straightforward interfacial magnetic ground-state structure (the  $A1$  configuration) whereby the manganite layer with the highest doping has the strongest magnetic response. Clearly, our conclusions on the magnetic ground-state are not *ab initio* as they involve significant experimental input. In our opinion, the unsatisfactory situation vis a vis choosing the  $U$  value is due to the limitations of the single-particle DFT+ $U$  method itself when applied to a complex and strongly correlated electronic system such as manganites: the theory is not accurate enough for the material, so some level of empiricism is unfortunately necessary.

### **Acknowledgments**

We are grateful to useful discussions with Carlos A. F. Vaz, Jason Hoffman, Yaron Segal, Fred J. Walker, Alexie M. Kolpak and Charles H. Ahn. This work was supported primarily by the National Science Foundation under Contracts No. MRSEC DMR 0520495 and DMR 1119826 and in part by the facilities and staff of the Yale University Faculty of Arts and Sciences High Performance Computing Center and by the National Science Foundation under grant #CNS 08-21132 that partially funded acquisition of the facilities. Bulldog parallel clusters of the Yale High Performance Computing center and TeraGrid provided

computational resources.

### Appendix A: Tests of the virtual crystal approximation

We treat the  $A$ -site  $\text{La}_{1-x}\text{Sr}_x$  alloying in  $\text{La}_{1-x}\text{Sr}_x\text{MnO}_3$  with the virtual crystal approximation [21, 22]. This approximation involves replacing the two elements by a fictitious one whose electron number is  $(1-x)N_{\text{La}} + xN_{\text{Sr}}$ , where  $N_{\text{La}}$  and  $N_{\text{Sr}}$  are the number of electrons of the La and Sr pseudo atoms, respectively. We stress that i) since the magnetic properties originate from Mn  $d$ -electrons and  $A$ -site atoms serve to donate electrons, we expect that the virtual crystal approximation is reasonable to describe the magnetic phase transition of manganites in the random distribution; ii) since the chemical properties mainly depend on the valence electrons, the approximation we make here is expected to be also good for Ca and Ba, and iii) our choice of pseudo potential and valence electrons shown in Table I ensures a very smooth interpolation between La and Sr as their pseudo valence electrons and nuclear pseudo charges only differ by one elementary charge. We perform simple tests of 1:1 Sr-La alloying (i.e. 50% alloying) in a  $c(2 \times 2) \times 2$  unit cell and the results are compared to the  $x = 0.5$  virtual crystal approximation as shown in Table VII. We can see that virtual crystal approximation quantitatively reproduces the lattice constants and the energy differences between various magnetic orderings when compared to the calculation with “real” La and Sr atoms. The accuracy of magnetic energy differences is consistent with earlier work [23].

### Appendix B: The effects of $\text{SrTiO}_3$ substrate

Inclusion of  $\text{SrTiO}_3$  substrate in the simulation of  $\text{PbTiO}_3/\text{La}_{1-x}\text{Sr}_x\text{MnO}_3$  heterostructures is computationally intensive. In this section, we test the effects of  $\text{SrTiO}_3$  substrate on structural and magnetic properties on the  $\text{PbTiO}_3/\text{La}_{1-x}\text{Sr}_x\text{MnO}_3$  interface. We compare two calculations: one with three unit cells of  $\text{SrTiO}_3$  and the other without  $\text{SrTiO}_3$ .  $\text{La}_{1-x}\text{Sr}_x\text{MnO}_3$  is four unit cells thick with nominal doping  $x = 0.2$ .  $\text{PbTiO}_3$  thin film is polarized so that both calculations are in the accumulation state. In terms of structural properties, we focus on two important quantities. One is the  $c/a$  ratio of each oxygen octahedron that encloses Mn atoms. The other is the rumpling  $\delta$  of each  $\text{MnO}_2$  layer. The

TABLE VII: Comparison between the virtual crystal approximation and supercell calculations. The nominal doping  $x$  is 0.5 in the virtual crystal approximation. A  $c(2 \times 2) \times 2$  supercell is employed with La and Sr atoms forming a checker-board pattern (every nearest neighbor of Sr is La and vice versa). The lattice constants reported are those for  $A$ -type antiferromagnetic ordering.  $\Delta E$  is the energy difference between ferromagnetic ordering and  $A$ -type antiferromagnetic ordering per Mn atom, defined by Eq. (1). A range of Hubbard  $U$  ( $0 \leq U \leq 2$  eV) are tested.

$U$ (eV)	Virtual crystal approximation						$c(2 \times 2) \times 2$ supercell							
	$a$ (Å)		$b$ (Å)		$c$ (Å)		$\Delta E$ (meV)	$a$ (Å)		$b$ (Å)		$c$ (Å)		$\Delta E$ (meV)
	$F$	$A$	$F$	$A$	$F$	$A$		$F$	$A$	$F$	$A$	$F$	$A$	
0	5.345	5.363	7.561	7.385	5.386	5.408	-34	5.327	5.366	7.482	7.372	5.381	5.411	-37
1	5.385	5.376	7.612	7.411	5.430	5.433	-10	5.355	5.380	7.513	7.398	5.400	5.439	-11
2	5.401	5.380	7.623	7.422	5.434	5.452	7	5.365	5.387	7.520	7.411	5.410	5.452	6

results are shown in Fig. 11A. Layer 1 is the interface. Layer 4 is the artificial surface when  $\text{SrTiO}_3$  is absent. The solid symbols are with  $\text{SrTiO}_3$  and the open symbols are without  $\text{SrTiO}_3$ . We can see that the structural properties with or without  $\text{SrTiO}_3$  substrate quickly converge as the interface is approached. At Layer 1, the difference is negligible. In terms of magnetic properties, we calculate the  $d$ -orbital magnetic moment of each Mn atom, using the Löwdin orbitals approach [16]. Fig. 11B shows the comparison between with  $\text{SrTiO}_3$  substrate (solid symbols) and without  $\text{SrTiO}_3$  substrate (open symbols). Similar to structural properties, the effects of  $\text{SrTiO}_3$  substrate on magnetic properties are generally very small and diminish at the interface. Therefore we do not include  $\text{SrTiO}_3$  substrate in our simulation, not only to reduce the computation burden but also to introduce an artificial surface so that we can apply a counting method (see Appendix C) to accurately calculate hole distribution in  $\text{La}_{1-x}\text{Sr}_x\text{MnO}_3$ .

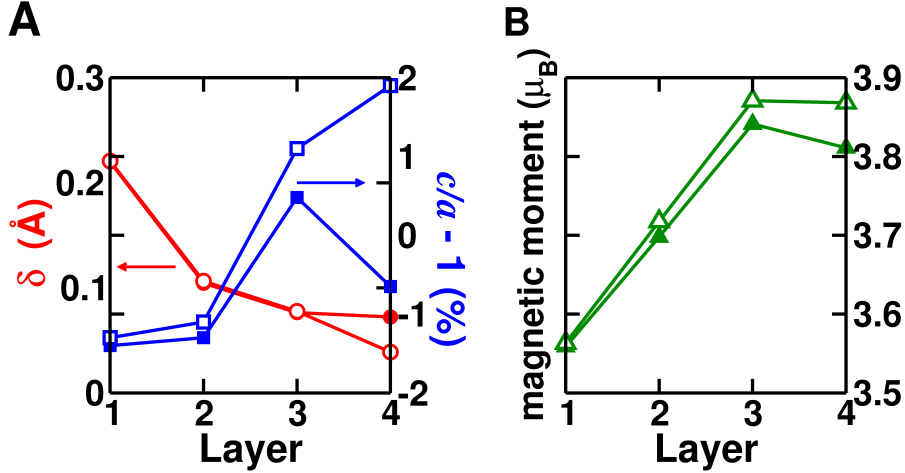


FIG. 11: (Color online) The effects of SrTiO<sub>3</sub> substrate on structural and magnetic properties at the PbTiO<sub>3</sub>/La<sub>1-x</sub>Sr<sub>x</sub>MnO<sub>3</sub> interface. Layer1 is the interfacial layer of MnO<sub>2</sub>. The solid symbols correspond to the data with SrTiO<sub>3</sub> substrate. The open symbols correspond to the data without SrTiO<sub>3</sub> substrate. **A)** rumplings of each MnO<sub>2</sub> layer and  $c/a$  ratio of each oxygen octahedron that encloses Mn atoms. **B)**  $d$ -orbital magnetic moment of each Mn atom, calculated by using Löwdin orbitals.

### Appendix C: The method for counting holes

A widely used approach for calculating the number of holes and the magnetization of Mn atoms is to use Löwdin orbitals [16]. However, a more direct method is to use the electron density itself. The difficulty lies in that the boundary between each manganite layer is not well-defined in the thin film of La<sub>1-x</sub>Sr<sub>x</sub>MnO<sub>3</sub>. We develop a method to self-consistently set the boundary between each manganite layer, provided that the manganite is half-metallic.

For a half-metallic manganite, there are no states at the Fermi level in the minority spin channel, so that there must be a definite integer number of electrons  $N_c$  filled in the minority spin channel.  $N_c$  depends on the details of pseudopotentials. For our pseudo atoms (see Table I), for doping level  $x$ , we have La<sup>3+</sup>:  $5s^25p^65d^06s^0$ , Sr<sup>2+</sup>:  $4s^24p^65s^0$ , O<sup>2-</sup>:  $2s^22p^6$  and due to charge conservation, Mn ion is nominally  $+(3+x)$  with an electron configuration  $3s^23p^63d^{4-x}4s^0$ . For one unit cell of La<sub>1-x</sub>Sr<sub>x</sub>MnO<sub>3</sub>, since spin polarization only comes from the electrons on Mn  $d$ -orbitals, we can sum all the other electrons that are formally spin unpolarized:  $8 \times (1-x) + 8 \times x + 8 \times 3 + 8 = 40$ . The four terms are from La<sup>3+</sup>, Sr<sup>2+</sup>, three O<sup>2-</sup> and the Mn ion without  $d$ -electrons. Hence  $N_c = 40/2 = 20$ , which is independent of

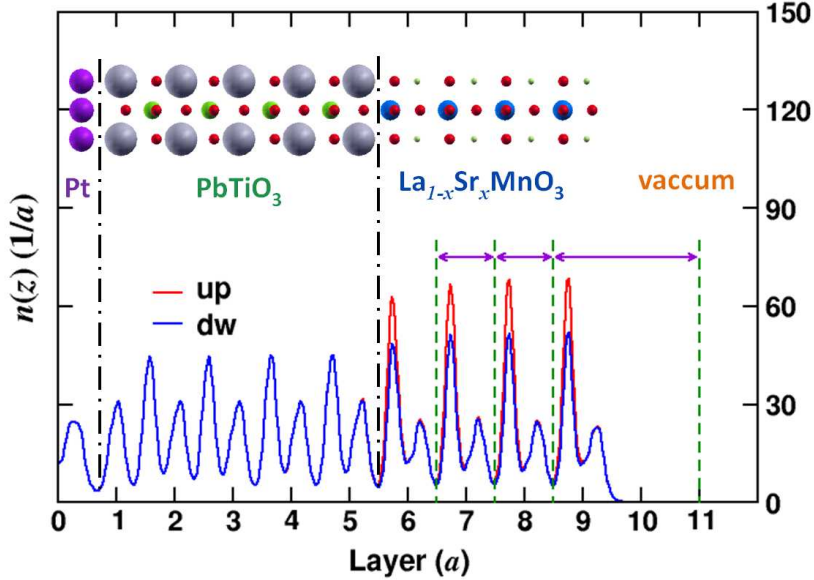


FIG. 12: (Color online) Illustration of how to count the charge in each layer of  $\text{La}_{1-x}\text{Sr}_x\text{MnO}_3$ . The spin polarized part is  $\text{La}_{1-x}\text{Sr}_x\text{MnO}_3$ . The green dashed lines highlight the computed boundaries of each layer.

hole doping. Now we start from the vacuum (see Fig. 12) where there is no charge. We integrate the minority spin channel moving into the film until the integral is equal to 20. Then this position determines the boundary of the first layer. Next we restart the integral from this boundary until it reaches 20 again. This determines the boundary of the second layer. Repeating the procedure yields the boundaries of each manganite layer. Once the boundaries are determined, we integrate the charge density of both majority and minority spins in each layer and thus layer-resolved holes and magnetization follow straightforwardly.

We comment that in DFT calculations, as long as the Hubbard  $U$  is larger than a critical value  $U_c$ , the manganites become half-metallic in the ferromagnetic phase. For  $\text{SrTiO}_3$ -strained  $Pnma$   $\text{La}_{1-x}\text{Sr}_x\text{MnO}_3$ , we find  $U_c \simeq 1$  eV. Therefore, for the useful and reasonable range of  $U$ , our method is valid.



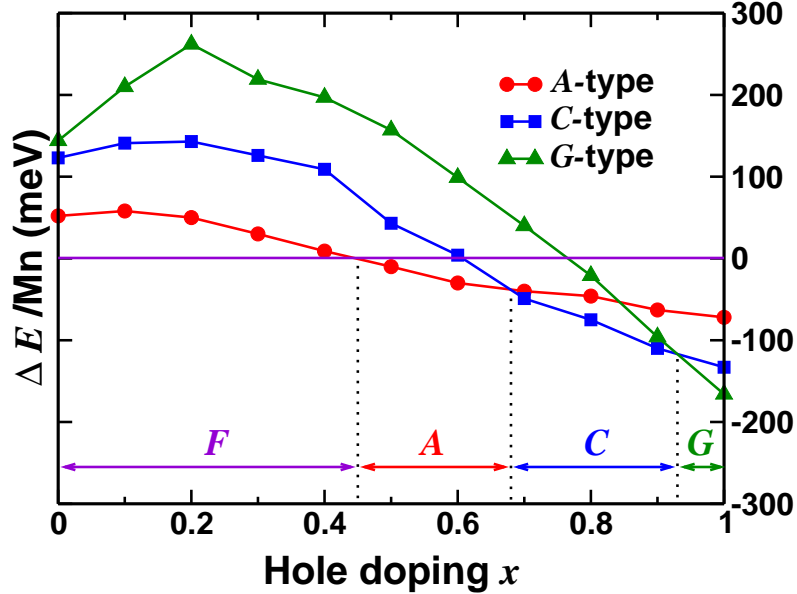


FIG. 13: (Color online) The complete magnetic phase diagram of  $\text{La}_{1-x}\text{Sr}_x\text{MnO}_3$  (4 formula, 20 atoms). The calculation is based on LSDA+ $U$  with  $U = 1$  eV.  $\Delta E$  is the energy difference between ferromagnetism and various types of anti-ferromagnetism. The labels  $F$ ,  $A$ ,  $C$  and  $G$  refer to ferromagnetism,  $A$ -type,  $C$ -type and  $G$ -type antiferromagnetism, respectively. Each label highlights the ground state magnetic structure of the given hole doping region.

#### Appendix D: The phase diagram of manganites from LSDA+ $U$

In this section, we provide the complete magnetic phase diagram of  $\text{La}_{1-x}\text{Sr}_x\text{MnO}_3$  in Fig. 13 based on LSDA+ $U$  with  $U = 1$  eV. In the high doping region ( $x > 0.4$ ), LSDA+ $U$  does reproduce the experimentally observed sequence of different magnetic ground states [23]: FM  $\rightarrow$   $A$  – AFM  $\rightarrow$   $C$  – AFM  $\rightarrow$   $G$  – AFM as the hole doping  $x$  increases. Our result is consistent with previous calculations [12].

#### Appendix E: Test of band alignment and possible artificial charge spillage

Due to the well known underestimation of band gaps in DFT calculations, band alignment errors and possible artificial charge spillage into the conduction bands of on material at an interface may occur. These errors can lead to unrealistic ground states when simulating the interface between ferroelectrics and metals [37]. We check our calculations of

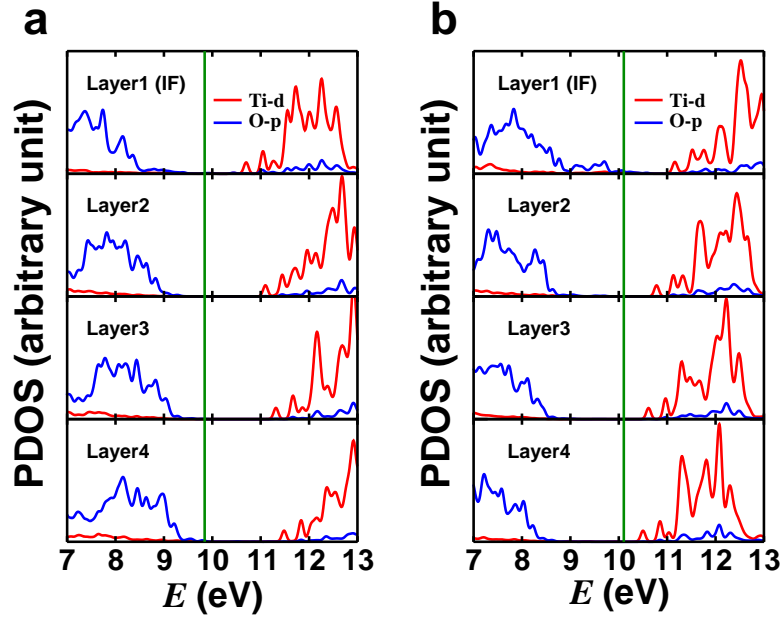


FIG. 14: (Color online) Atomic projected density of states (PDOS) of  $\text{PbTiO}_3$  in the  $\text{PbTiO}_3/\text{La}_{1-x}\text{Sr}_x\text{MO}_3/\text{Pt}$  heterostructures. **a)** The accumulation state. **b)** The depletion state. The red curves are Ti- $d$  projected states and the blue curves are O- $p$  projected states. Layer1 refers to the interface between  $\text{PbTiO}_3$  and  $\text{La}_{1-x}\text{Sr}_x\text{MnO}_3$  (the interface we are interested in) and Layer4 is the interface between  $\text{PbTiO}_3$  and Pt. The green solid line is the Fermi level.

$\text{PbTiO}_3/\text{La}_{1-x}\text{Sr}_x\text{MO}_3/\text{Pt}$  interface and find that the Fermi level is in the band gap of  $\text{PbTiO}_3$ . A typical projected density of states (PDOS) of both the accumulation and depletion states is illustrated in Fig. 14, where Layer1 refers to the interface between  $\text{PbTiO}_3$  and  $\text{La}_{1-x}\text{Sr}_x\text{MnO}_3$  (the interface we are interested in) and Layer4 is the interface between  $\text{PbTiO}_3$  and Pt. We can see that the interior of  $\text{PbTiO}_3$  remains insulating. We need to point out that both terminations of  $\text{PbTiO}_3$  are PbO layers in our calculations, instead of the pathological  $\text{TiO}_2$  termination which leads to a metallic ferroelectric ground state in other similar systems [37].

- 
- [1] W. Eerenstein, N. D. Mathur, and J. F. Scott, *Nature* **442**, 759 (2006).
- [2] R. Ramesh and N. A. Spaldin, *Nat. Mater.* **6**, 21 (2007).
- [3] K. F. Wang, J. M. Liu, and Z. F. Ren, *Adv. Phys.* **58**, 321 (2009).
- [4] C. A. F. Vaz, J. Hoffman, C. H. Ahn, and R. Ramesh, *Advanced Materials* **22**, 2900 (2010).
- [5] I. Dzyaloshinskii, *Soviet Phys. J. Expt. Theor. Phys.* **10**, 628629 (1960).
- [6] G. Srinivasan, E. T. Rasmussen, J. Gallegos, R. Srinivasan, Y. I. Bokhan, and V. M. Laletin, *Phys. Rev. B* **64**, 214408 (2001).
- [7] N. A. Spaldin and M. Fiebig, *Science* **309**, 391 (2005).
- [8] C.-G. Duan, S. S. Jaswal, and E. Y. Tsymbal, *Phys. Rev. Lett.* **97**, 047201 (2006).
- [9] K. Yamauchi, B. Sanyal, and S. Picozzi, *Appl. Phys. Lett.* **91**, 062506 (2007).
- [10] M. K. Niranjana, J. P. Velev, C.-G. Duan, S. S. Jaswal, and E. Y. Tsymbal, *Phys. Rev. B* **78**, 104405 (2008).
- [11] J. M. Rondinelli, M. Stengel, and N. A. Spaldin, *Nat. Nanotech.* **3**, 46 (2008).
- [12] J. D. Burton and E. Y. Tsymbal, *Phys. Rev. B* **80**, 174406 (2009).
- [13] C. A. F. Vaz, J. Hoffman, Y. Segal, J. W. Reiner, R. D. Grober, Z. Zhang, C. H. Ahn, and F. J. Walker, *Phys. Rev. Lett.* **104**, 127202 (2010).
- [14] V. Garcia, S. Fusil, K. Bouzehouane, S. Enouz-Vedrenne, N. D. Mathur, A. Barthelemy, and M. Bibes, *Nature* **460**, 81 (2009).
- [15] N. C. Bristowe, M. Stengel, P. B. Littlewood, J. M. Pruneda, and E. Artacho, *Phys. Rev. B* **85**, 024106 (2012).
- [16] P.-O. Löwdin, *J. Chem. Phys.* **18**, 365 (1950).
- [17] M. C. Payne, M. P. Teter, D. C. Allan, T. A. Arias, and J. D. Joannopoulos, *Rev. Mod. Phys.* **64**, 1045 (1992).
- [18] D. Vanderbilt, *Phys. Rev. B* **41**, 7892 (1990).
- [19] W. Kohn and L. J. Sham, *Phys. Rev.* **140**, A1133 (1965).
- [20] V. I. Anisimov, F. Aryasetiawan, and A. I. Lichtenstein, *J. Phys.: Condens. Matter* **9**, 767 (1997).
- [21] L. Nordheim, *Ann. Phys. (Leipzig)* **9**, 607 (1931).
- [22] L. Bellaiche and D. Vanderbilt, *Phys. Rev. B* **61**, 7877 (2000).

- [23] Z. Fang, I. V. Solovyev, and K. Terakura, Phys. Rev. Lett. **84**, 3169 (2000).
- [24] Y. Nohara, A. Yamasaki, S. Kobayashi, and T. Fujiwara, Phys. Rev. B **74**, 064417 (2006).
- [25] G. Trimarchi and N. Binggeli, Phys. Rev. B **71**, 035101 (2005).
- [26] C. Zener, Phys. Rev. **82**, 403 (1951).
- [27] Y. Tokura, Rep. Prog. Phys. **69**, 797 (2006).
- [28] H. A. Kramers, Physica **1**, 182 (1934).
- [29] A. Sadoc, B. Mercey, C. Simon, D. Grebille, W. Prellier, and M.-B. Lepeitit, Phys. Rev. Lett. **104**, 046804 (2010).
- [30] I. V. Solovyev, Phys. Rev. B **69**, 134403 (2004).
- [31] I. Solovyev, N. Hamada, and K. Terakura, Phys. Rev. Lett. **76**, 4825 (1996).
- [32] P. W. Anderson and H. Hasegawa, Phys. Rev. **100**, 675 (1955).
- [33] T. Hashimoto, S. Ishibashi, and K. Terakura, Phys. Rev. B **82**, 045124 (2010).
- [34] M. Cococcioni and S. de Gironcoli, Phys. Rev. B **71**, 035105 (2005).
- [35] H. J. Kulik, M. Cococcioni, D. A. Scherlis, and N. Marzari, Phys. Rev. Lett. **97**, 103001 (2006).
- [36] R. D. King-Smith and D. Vanderbilt, Phys. Rev. B **47**, 1651 (1993).
- [37] M. Stengel, P. Aguado-Puente, N. A. Spaldin, and J. Junquera, Phys. Rev. B **83**, 235112 (2011).
- [38] See <http://www.quantum-espresso.org>
- [39] The original Ising model with Hamiltonian of the form  $\sum_{ij} J_{ij} S_i S_j$  can not be justified rigorously from first principles here because our system is metallic and there are no isolated spins. Instead, we use layer-resolved magnetization  $m_i$  as a basis variable to create an effective model for our system which has the form of an Ising Hamiltonian.
- [40] We used a Löwdin orbital analysis and found that the change in the hole spatial distribution between different magnetic structures is insignificant. However, just as we argued in the appendix, the Löwdin method itself is not highly accurate and can only be considered to provide indirect evidence.